Materials Advances

ROYAL SOCIETY OF CHEMISTRY

PAPER

View Article Online
View Journal

Check for updates

Cite this: DOI: 10.1039/d5ma00760g

Exploring facet-engineered anatase nanoparticles for amplification of sensitivity in heavy metal ion detection and other applications

Md. Anayet Ullah,[ab] Fataha Nur Robel,[b] Newaz Mohammed Bahadur,[c] Dipa Islam,[d] Subarna Sandhani dey,[e] Samina Ahmed *[a] and Md. Sahadat Hossain *[a]

Received 15th July 2025,
Accepted 2nd December 2025

DOI: 10.1039/d5ma00760g

rsc.li/materials-advances

TiO_2 is one of the most extensively studied nanomaterials due to its remarkable surface, catalytic, and electronic properties, which are further enhanced when synthesized with exposed facets. In this study, anatase-phase TiO_2 nanoparticles with different crystal facets were synthesized using inorganic modifiers through a hydrothermal method. The synthesized samples were characterized using various analytical techniques. X-ray diffraction (XRD), Fourier transform infrared spectroscopy (FTIR), and Raman spectroscopy confirmed the formation of anatase TiO_2. The crystallite size, estimated from XRD data, ranged between 1–50 nm, except for the linear straight-line method (LSLM), which exhibited a higher value. Growth preference, texture coefficient and Raman data and structural analysis verified the facet formation. Additionally, thermogravimetric analysis (TGA) revealed enhanced thermal stability of the samples. Photocatalytic studies demonstrated that {001}-faceted and {101}/{001} co-faceted TiO_2 achieved complete degradation of Congo Red (CR) dye within 30 min, significantly outperforming {101}-faceted TiO_2 (69.36% degradation). Scavenging experiments confirmed that $^{\bullet}OH$ radicals played the dominant role in CR degradation over the {001}-faceted TiO_2. Kinetic studies based on the Langmuir–Hinshelwood model revealed apparent rate constants of 0.0202 min^{-1} for {101}-faceted TiO_2, 0.0081 min^{-1} for {001}-faceted TiO_2, and 0.0127 min^{-1} for {101}/{001}-co-faceted TiO_2. Furthermore, {001}-faceted TiO_2 exhibited significant antimicrobial efficacy against Gram-positive bacteria, attributed to enhanced surface activity. Electrochemical studies revealed the superior sensing capabilities of {001}-faceted TiO_2 for Pb^{2+} ion detection, with its enhanced electroactive surface area contributing to a limit of detection (LOD) of 9.378 ppm and a limit of quantification (LOQ) of 31.162 ppm.

Introduction

Nowadays, nanomaterials are widely valued for their exceptional properties over bulk materials. For example, nanostructured titanium dioxide (TiO_2), with its remarkable optical and electronic features, has revolutionized applications in photocatalysis, sensors, photovoltaics, and photonic devices.[1] This affordable, non-toxic, and stable semiconductor is extensively used in dye sensitized solar cells,[2] pollutant remediation,[3] charge spreading devices,[4] gas sensors,[5] photocatalytic degradation, photoluminescence,[6] bactericides,[7] optical coatings,[8] opto-electronic devices,[9] electrochemistry,[10] textiles[11] *etc.* TiO_2 is found predominantly in three crystalline forms: anatase, brookite, and rutile. Anatase is notable for its high catalytic efficiency, attributed to its vast surface area, minimal charge recombination, strong oxygen affinity, and broad bandgap, making it highly effective under UV light.[12] The performance of TiO_2 is influenced by its physical and chemical properties, including crystal structure, grain size, morphology, and surface characteristics, prompting interest in synthesizing TiO_2 with specific crystal structures to enhance highly photoactive facets. Different facets of a single crystal exhibit distinct properties, affecting reactivity.[13] Anatase TiO_2, with its wide band gap, demonstrates photocatalytic activity through photogenerated electrons (e^-) and holes (h^+) at the surface, initiating redox reactions. However, electron–hole recombination during transport reduces carrier efficiency, with charge separation relying

---

[a] *Institute of Glass & Ceramic Research and Testing, Bangladesh Council of Scientific and Industrial Research (BCSIR), Dhaka 1205, Bangladesh. E-mail: shanta_samina@yahoo.com, saz8455@gmail.com*

[b] *Department of Applied Chemistry and Chemical Engineering, Noakhali Science and Technology University, Noakhali, Bangladesh*

[c] *Department of Chemistry, Noakhali Science and Technology University, Noakhali 3814, Bangladesh*

[d] *Biomedical and Toxicological Research Institute, Bangladesh Council of Scientific and Industrial Research (BCSIR), Dhaka 1205, Bangladesh*

[e] *Institute of Food Science and Technology, Bangladesh Council of Scientific and Industrial Research (BCSIR), Dhaka 1205, Bangladesh*

on trapping holes by H_2O or electrons by O_2. Surface properties, such as crystal facets, defects, and adsorbed ions, impact charge migration, making the modification of TiO_2 crystal facets a key focus.[14] Moreover, TiO_2 encounters limitations such as a broad band gap, low quantum yield, and swift recombination of photogenerated charges, which constrain its visible light absorption and hinder large-scale applications. In recent years, facet engineering of TiO_2 crystals has gained prominence as an effective strategy to boost photocatalytic efficiency.[15]

Various methods, including sputtering,[16] aerosol pyrolysis,[17] MOCVD,[18] electrodeposition,[19] spray pyrolysis,[20] sol–gel,[21] and hydrothermal synthesis,[22] have been employed to fabricate TiO_2 nanostructured thin films. Among these, hydrothermal synthesis is particularly favored for its simplicity, cost-effectiveness, and ability to produce well-aligned nanostructures with a high surface area. It also allows for the straightforward synthesis of single-crystalline materials.[23] Hydrothermal or solvothermal techniques typically operate at temperatures below 1000 °C, offering energy efficiency compared to alternative approaches like chemical vapor deposition, which often require higher temperatures. These methods provide precise control over the morphology and crystallinity of TiO_2, making them ideal for photocatalysis and sensing applications.[24]

For TiO_2, the primary low-index facets are {101}, {001}, and {100}. Among these, the {001} facet of anatase TiO_2 is particularly reactive due to its high surface energy (0.90 J m^{-2}), which exceeds that of the {100} (0.53 J m^{-2}) and {101} (0.44 J m^{-2}) facets, making it a key player in photocatalytic applications.[25] However, due to its thermodynamic instability, the {001} facet is rarely exposed in large quantities, with most natural and synthesized TiO_2 crystals predominantly showing the {101} facet. The reactivity of the {001} facet, characterized by low atomic coordination and active surface oxygen atoms, facilitates efficient dissociative adsorption of reactant molecules, making it ideal for photocatalytic processes such as the degradation of organic pollutants including various dyes.[26] Among these, Congo Red (CR) is frequently selected in photocatalytic studies due to its highly stable complex aromatic azo structure, which makes it persistent in water and resistant to natural degradation. Its metabolites, including benzidine, are toxic, exhibiting carcinogenic and mutagenic properties, and can trigger allergic reactions, increase chemical oxygen demand in water bodies, and even contribute to infertility. These characteristics make CR considerably more difficult to degrade, establishing it as a rigorous benchmark for evaluating photocatalytic performance.[27,28] Recent research has focused on manipulating TiO_2 crystal facets to enhance photocatalytic performance, particularly by increasing the exposure of {001} facets, which are essential for trapping holes as oxidative sites. However, some studies have also reported that {101} facets exhibit higher photocatalytic activity than {001} facets in certain applications.[29]

In addition to organic pollutants, the increasing levels of heavy metal contaminants have drawn significant public and scientific concern due to their toxicity, bioaccumulation, and persistence in ecosystems.[30] Heavy metals such as lead (Pb^{2+}), cadmium (Cd^{2+}), and mercury (Hg^{2+}) pose severe health risks, including neurological disorders, organ damage, and carcinogenic effects.[31] In recent years, electrochemical sensors have gained widespread attention in chemical and biological studies due to their high sensitivity, simplicity, cost-effectiveness, and reliability in detecting trace pollutants.[32] Various analytical techniques, including atomic absorption spectroscopy (AAS),[33] inductively coupled plasma mass spectrometry (ICP-MS),[34] and X-ray fluorescence (XRF)[35] are commonly used for the detection and quantification of heavy metals. However, these methods often require expensive instrumentation, complex sample preparation, and time-consuming preconcentration procedures.[36] Among electrochemical techniques, anodic stripping voltammetry (ASV) has emerged as a powerful and widely applied method for detecting heavy metal ions in water. ASV offers high sensitivity, accuracy, low cost, and the ability to detect multiple metal ions simultaneously.[37] The technique involves an initial preconcentration step, where metal ions accumulate on an electrode surface, followed by a stripping step, during which the deposited metals are reoxidized, producing measurable current signals proportional to metal ion concentration.[38] This makes ASV a highly efficient, rapid, and environmentally friendly approach for monitoring heavy metal contamination in water sources, offering advantages over traditional detection techniques.[39]

Beyond their application in photocatalysis and electrochemical sensing, TiO_2 nanoparticles have also demonstrated significant antimicrobial properties. The antimicrobial mechanism primarily involves direct interaction with bacterial cell walls, leading to structural changes, increased membrane permeability, and eventual cell death.[40]

In this study, anatase-phase TiO_2 nanoparticles with various exposed crystal facets were synthesized using inorganic modifiers such as NH_4Cl, NH_4SO_4, and HF. The synthesized TiO_2 samples were thoroughly characterized using a range of techniques, and the influence of facet modification on their photocatalytic, antimicrobial, and electrochemical properties was further investigated. The photocatalytic degradation of Congo Red (CR) dye was evaluated, alongside antimicrobial activity, to assess the material's effectiveness in environmental pollutant removal and microbial inhibition. Additionally, electrochemical sensors for the detection of Pb^{2+} ions were fabricated using the synthesized TiO_2, targeting heavy metal sensing applications. These investigations aim to enhance the understanding of how facet modification can tune TiO_2's properties, thereby improving its performance in environmental remediation and sensing applications.

Materials and methods

Materials and equipment

Tetrabutyl orthotitanate (purity 98%) was acquired from Tokyo Chemical Industry Co. Ltd, Japan. Ammonium chloride (purity 99%), hydrofluoric acid (purity 48%), sulfuric acid (purity 99%), ammonia (purity 25%) and isopropanol were acquired from

Merck, Germany. Crystallographic analysis was performed using a Rigaku XRD instrument with Cu Kα X-rays (λ = 1.5406 Å) at 40 kV and 50 mA, with a cooling temperature of 23 °C. Functional groups were analyzed *via* FT-IR spectroscopy using an IR-Prestige 21 spectrometer, scanning from 400 to 4000 cm^{-1} with a resolution of 4 cm^{-1} and 30 scans. Thermal analysis was conducted using STA equipment in a nitrogen atmosphere, ranging from 50 °C to 800 °C. Structural and elemental characterization was done using a JEOL JSM-7610F field emission scanning electron microscope (FESEM) with integrated energy-dispersive X-ray spectroscopy (EDX) capabilities at 25 kV and SEM, EVO-18, Carl Zeiss, Germany machine.

Experimental methods

Synthesis of different crystal plane faceted TiO_2. For the synthesis of {101}-faceted TiO_2, 2 g of tetrabutyl orthotitanate (TBOT) was dispersed in a solution composed of 15 mL DI water and 15 mL isopropanol. Subsequently, 0.2 g of NH_4Cl was introduced into the reaction mixture, which was stirred and ultrasonicated to achieve a uniform dispersion. The prepared suspension was then transferred to a Teflon-lined autoclave, sealed, and heated at 180 °C for 24 hours under hydrothermal conditions. Upon completion of the reaction, the solid product was recovered through filtration, followed by extensive washing with DI water and a single wash with ethanol to eliminate residual impurities. Finally, the cleaned product was dried in an oven at 105 °C, yielding the desired {101}-faceted TiO_2. Fig. S1 shows the schematic depiction of the synthesis procedure of {101}-faceted TiO_2.

For the synthesis of {001}-faceted TiO_2, 8.33 mL of TBOT was mixed with 1 mL of HF in a dry Teflon-lined autoclave and heated at 180 °C for 24 hours under hydrothermal conditions. Upon the reaction's completion, the product was recovered through filtration, followed by extensive washing with water and a single wash with ethanol to remove residual impurities. To eliminate any remaining fluorine species, the product was further treated with an aqueous NaOH solution, followed by additional washing with deionized water. Finally, the purified material was dried in an oven at 105 °C, yielding {001}-faceted TiO_2. Fig. S2 shows the schematic depiction of the synthesis procedure of {001}-faceted TiO_2.

For the synthesis of {101}/{001} co-faceted TiO_2, 2 g of TBOT was dissolved in a mixture of 15 mL deionized water and 15 mL isopropanol. Subsequently, 0.5 g $(NH_4)_2SO_4$ was added to the reaction mixture, followed by stirring and ultrasonication to ensure uniform dispersion. The subsequent steps mirrored the synthesis of {101}-faceted TiO_2. Fig. S3 shows the schematic depiction of the synthesis procedure of {101}/{001} co-faceted TiO_2.

The $(NH_4)_2SO_4$ used to prepare the {101}/{001} co-faceted TiO_2 was synthesized by adding diluted H_2SO_4 dropwise to an NH_3 solution under continuous stirring. The addition of H_2SO_4 was carefully monitored until the solution reached a neutral pH of 7. The resulting solution was then heated to 50 °C to facilitate water evaporation. Once crystals formed, the remaining water was removed by drying the crystals in a vacuum oven at 50 °C. The crystals were subsequently crushed using a mortar and pestle to obtain a powder.

Photocatalytic assessment. The photocatalytic assessment was conducted using Congo Red (CR) dye as a model pollutant, with a 40 mL solution of 10 ppm CR dye and a sample weight of 0.05 g. A 500 W SEN TAI JM-500 halogen lamp was used as the visible light source, with the sample placed 0.14 m beneath the lamp. The temperature in the irradiation chamber was maintained at 25 °C using a cooling water circulation system. The concentration of the dye was measured using a Hitachi U-910 UV-vis spectrometer, after the assessment. The degradation percentage was calculated using the following formula:[41]

$$\text{Degradation percentage} = \frac{C_0 - C_t}{C_0} \times 100\% \qquad (1)$$

Here, C_0 is the concentration at the beginning, C_t is the concentration of the synthesized sample at a particular time, t.

Scavenging experiments were carried out using 2-propanol (isopropyl alcohol) and ethylenediaminetetraacetic acid (EDTA) as scavengers for hydroxyl radicals ($^{\bullet}OH$) and photogenerated holes (h^+), respectively. In each experiment, 10 mL of the scavenger solution was added to 40 mL of 10 ppm CR dye containing 0.05 g of the catalyst, followed by halogen irradiation for 30 min. The reusability of the catalyst was evaluated under identical conditions over five consecutive cycles.[42] After each cycle, the catalyst was decanted, washed three times with water, dried at 60 °C for 6 h, and reused with a fresh dye solution.

Antimicrobial activity. The synthesized samples were tested for antimicrobial efficacy against two Gram-positive bacteria (*L. monocytogenes* ATCC 13932, *S. aureus* ATCC 6538), two Gram-negative bacteria (*S. abony* NCTC 6017, *E. coli* ATCC 25922), and a fungal strain, *C. albicans* ATCC 10342. For the assay, 50 mg of each sample was dissolved in distilled water containing 2% Tween 20 (Promega, USA). Chloramphenicol served as the positive control for antibacterial activity, while Azoxystrobin was used as the positive control for antifungal activity. The experiment was carried out using the agar-well diffusion method, where a fresh microbial culture was evenly spread onto the agar surface. Using an sterile cotton bud, 6 mm diameter wells were carefully created on the agar plate. The prepared sample solutions were then introduced into each well to assess antimicrobial effectiveness. The plates were stored at 4 °C for 3 hours to ensure uniform dispersion of the sample particles, then incubated at 37 °C for 24 hours, after which the inhibition zones were observed and their diameters measured.

Electrochemical experiment. Electrochemical experiments were conducted using the CS300 (Corrtest, China) with a three-electrode system: Pt as the counter electrode, Ag/AgCl as the reference, and a modified glassy carbon (GC) electrode as the working electrode. The modification of the GC electrode was carried out using a mixture of {001}-modified TiO_2 sample, carbon black (CB) as a conducting agent, polyvinylidene fluoride (PVDF) as a binder, and *N*-methyl pyrrolidone (NMP) as a volatile solvent. The composition of the mixture was as follows:

70% TiO_2 sample, 20% CB, and 10% PVDF. NMP was used to dissolve PVDF and facilitate uniform mixing.

Results

Characterization

The XRD diffractogram of the synthesized TiO_2 samples, shown in Fig. 1, was compared with the standard ICDD database for anatase (card no: #00-021-1272). The anatase phase, belonging to the tetragonal crystal system with the space group $I41/amd$ (141), is characterized by prominent peaks at 2θ values of 25.28° (1 0 1), 37.80° (0 0 4), 48.05° (2 0 0), and 53.89° (1 0 5). The synthesized samples exhibited slight variations: the {101}-faceted TiO_2 showed peaks at 25.35°, 37.73°, 47.84°, and 54.40°; the {001}-faceted TiO_2 at 25.21°, 37.90°, 47.92°, and 53.75°; and the {101}/{001} co-faceted TiO_2 at 25.30°, 37.89°, 47.89°, and 54.11°. These results demonstrate strong agreement with the standard anatase phase, confirming the successful synthesis of the desired crystal structure.

An evaluation of the crystal structure was performed by determining lattice parameters, crystallite size, dislocation density, and microstrain using eqn (E1)–(E5), with outcomes tabulated in Table 1.

Various crystallite parameters, such as size of the crystallite, intrinsic strain, stress, and energy density can be computed using XRD data by using different XRD models, comprising Scherrer's model, modified Williamson–Hall methods, the Monshi–Scherrer (M–S) model, the size-strain plot (SSP), and the Halder–Wagner (H–W) model. Each of these models considers different factors that affect the diffraction pattern, including peak broadening due to instrumental effects, internal strain, and stress, along with the isotropic or anisotropic nature of the crystal lattice. These factors significantly influence the XRD parameters owing to imperfections in the crystal structure, such as point defects, triple junctions, dislocations, grain boundaries, and stacking faults. These defects typically contribute to peak broadening and variations in lattice strain, which directly impact the accuracy of the crystallite size estimation. Thus, the application of multiple models allows for a more in-depth and precise calculation of the size of the crystallite and other parameters.[43] In Scherrer's model, the average size of the crystallite is estimated using the equation, crystallite size, $D = \dfrac{k\lambda}{\beta\cos\theta}$ and displayed in Table 1. The parameters obtained from other models are summarized in Table 2, while the corresponding plots are shown in Fig. S4–S10, with the corresponding equations available elsewhere.[44]

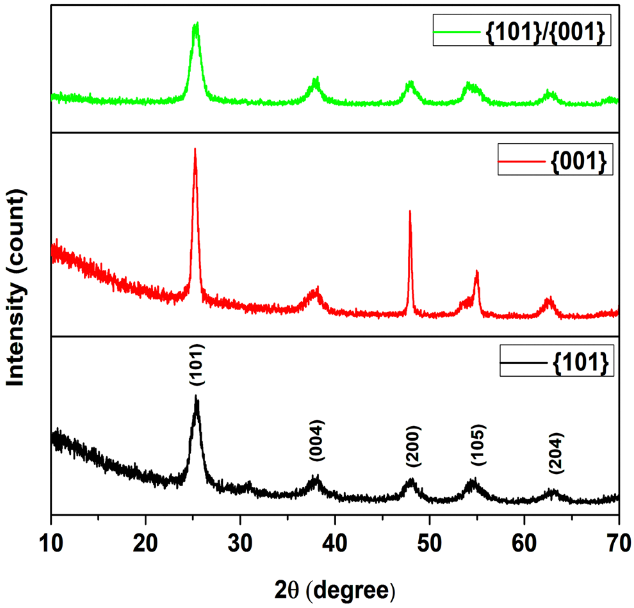

Fig. 1 XRD diffractogram of the synthesized TiO_2 samples.

Growth preference and texture coefficient are two key parameters used to assess whether a crystalline material exhibits growth in a specific exposed plane. Growth preference provides insights into the favorable growth direction along a specific crystallographic plane and can be estimated using the normalized intensity of that plane, as calculated with eqn (E6) and (E7). Here, negative values indicate a lower preference for growth on the specific plane, whereas positive values suggest that growth on this specific plane is thermodynamically stable. In contrast, the texture coefficient (T_c) is utilized to examine the actual growth direction of the crystallographic plane. Estimation of the texture coefficient was done using the peak intensities associated with the (101), (004), (200), and (105) planes, as recorded from the XRD data, employing eqn (E8). When $T_c(hkl)$ surpasses 1, it indicates that crystallites are more prevalently oriented in the (hkl) direction.

Table 3 presents the preferred growth values for the synthesized TiO_2 samples, while Table 4 shows the texturing behavior of the synthesized TiO_2 samples. For the {101}-faceted TiO_2, positive preferred growth values were observed for the (004) and (105) planes, suggesting a strong tendency for growth along the {001} and {101} directions, respectively. However, the texture coefficient indicates that texturing predominantly occurs along the {101} direction, as evidenced by the higher T_c value for the (105) plane, while the (004) plane shows a significantly lower T_c value. This correlation supports the conclusion that the sample predominantly exposes the (101) crystallographic direction, confirming the alignment of crystallites along this direction. In contrast, for the {001}-faceted TiO_2, a positive preferred growth value was found only for the (004) plane, and the texture coefficient for this plane exceeded 1. These findings confirm that the sample is mainly exposed along the {001} direction. Additionally, the {101}/{001}-co-faceted TiO_2 exhibited positive preferred growth values for both the (004) and (105) planes, with notable T_c values for both planes, confirming that this sample exhibits growth along both the {101} and {001} directions.

FT-IR is a highly effective and widely employed method for analyzing materials by identifying the functional groups embedded in their structure. Fig. 2 displays the FT-IR spectra of the synthesized TiO_2 samples. Absorption in the 400–700 cm^{-1} region, indicative of the stretching and bending vibrations of the

Table 1 Crystallographic parameters of the synthesized TiO_2 samples

Sample	Lattice parameters, Å	Size of crystallites, D (nm)	Dislocation density, δ (10^{15} lines per m^2)	Microstrain, ε	Crystallinity index
{101}	$a = b = 3.78$, $c = 9.53$	6.74	2.2	0.99	0.70
{001}	$a = b = 3.79$, $c = 9.49$	15.12	4.37	0.56	1.02
{101}/{001}	$a = b = 3.80$, $c = 9.49$	5.47	3.34	1.01	1.21

Table 2 Estimated crystallite property parameters of the synthesized TiO_2 samples

Name of model		Crystallite size, D (nm); strain, ε; stress, σ (N m^{-2}); energy density, μ (J m^{-3})		
		{101}	{001}	{101}/{001}
Williamson–Hall model	UDM	$\varepsilon = 0.0032$ $D = 7.62$	$\varepsilon = -0.0023$ $D = 5.52$	$\varepsilon = 0.0018$ $D = 5.68$
	USDM	$\sigma = 6.533 \times 10^8$ $D = 7.62$	$\sigma = -4.633 \times 10^8$ $D = 5.52$	$\sigma = 3.76 \times 10^8$ $D = 5.68$
	UDEDM	$\mu = 1.04 \times 10^6$ $D = 7.62$	$\mu = -5.22 \times 10^6$ $D = 5.52$	$\mu = 3.43 \times 10^5$ $D = 5.68$
M–S model		$D = 6.59$	$D = 10.93$	$D = 10.93$
SSP		$D = 6.25$ $\varepsilon = 0.0028$	$D = 5.35$ $\varepsilon = -0.004$	$D = 4.9$ $\varepsilon = 0.0014$
H–W model		$D = 45.05$ $\varepsilon = 0.005$	$D = 38.61$ $\varepsilon = -0.007$	$D = 35.09$ $\varepsilon = 0.002$
S–S model		$D = 7.70$	$D = 22.36$	$D = 5.78$

Table 3 Growth preference in the synthesized TiO_2 samples

Sample	Plane	Growth preference
{101}	101	−0.38
	004	0.46
	200	−0.04
	105	0.85
{001}	101	−0.14
	004	0.46
	200	−0.08
	105	−0.01
{101}/{100}	101	−0.30
	004	1.27
	200	−0.50
	105	0.66

Table 4 Texture coefficient in the synthesized TiO_2 samples

Sample	Plane (hkl)	Texture coefficient, (T_c)	Observation
{101}	101	0.6500	101 direction texturing
	004	1.1616	
	200	0.7928	
	105	1.3956	
{001}	101	0.8679	001 direction texturing
	004	1.3232	
	200	0.8571	
	105	0.9517	
{101}/{100}	101	0.6850	101 and 001 direction texturing
	004	1.6152	
	200	0.4511	
	105	1.2487	

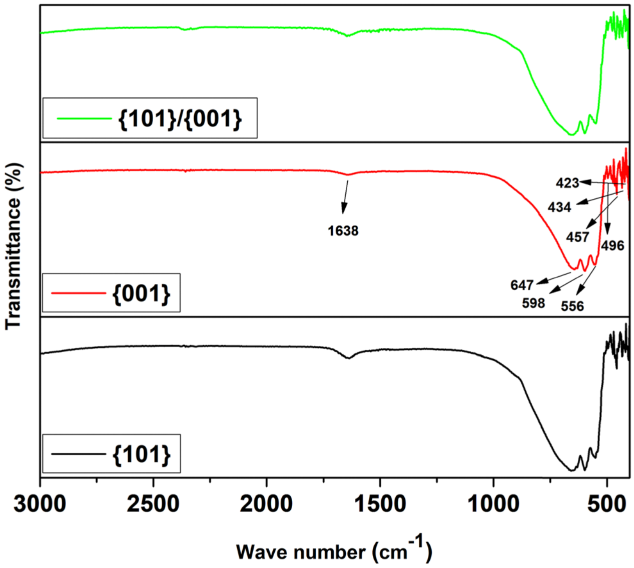

Fig. 2 FT-IR spectra of the synthesized TiO_2 samples.

Ti–O–Ti bond, was prominently observed in all samples, confirming its presence in the synthesized nanoparticles. Apart from this region, a peak around 1631 cm^{-1} was detected, attributed to the O–H bending vibrations (Ti–OH). For {001}-faceted TiO_2, the absorption peaks are prominent at 423, 434, 457, 496, 556, 598, 647, and 1631 cm^{-1}, with other samples showing close proximity to these values. Similar absorption peaks to those samples have been observed in previous literature.[45,46]

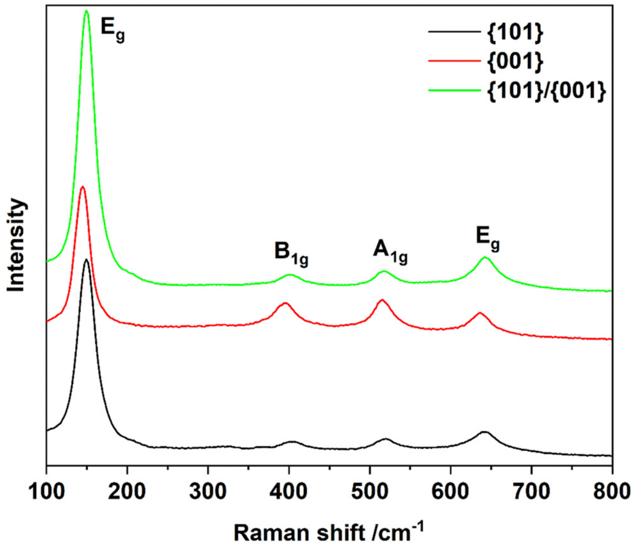

Fig. 3 Raman spectra of the synthesized TiO_2 samples.

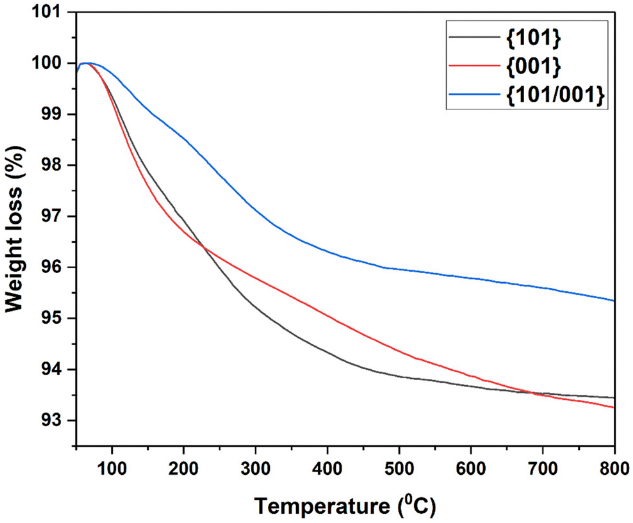

Fig. 4 Thermal weight loss of the synthesized TiO_2 samples.

The Raman spectra, illustrated in Fig. 3, demonstrate that all samples exhibit similar spectral profiles at approximately 144, 395, 516, and 636 cm^{-1}. The most intense peak, observed near 144 cm^{-1}, corresponds to the E_g vibrational mode of anatase. The band at 395 cm^{-1} is attributed to the B_{1g} mode, while the peak at 516 cm^{-1} results from the overlapping of the A_{1g} (513 cm^{-1}) and B_{1g} (519 cm^{-1}) modes of anatase. Additionally, the E_g mode at 636 cm^{-1} is also evident. The E_g peak results from O–Ti–O symmetric stretching, while the B_{1g} and A_{1g} modes arise from symmetric and asymmetric O–Ti–O bending, respectively.[47] Moreover, Tian *et al.*[48] suggested that the {001} facet percentage can be determined by analyzing the intensity of the 144 cm^{-1} and 516 cm^{-1} peaks as outlined in Table 5.

The heat response behavior of the synthesized TiO_2 particles was assessed by performing thermal weight loss analysis. The thermogram (Fig. 4) for the synthesized TiO_2 samples, heated from 50 °C to 800 °C under a controlled atmosphere, illustrates the weight-loss events occurring during the heating process. Both {101}-faceted and {001}-faceted TiO_2 samples exhibited a similar trend in the TGA curve, with nearly identical mass losses of 6.52% and 6.74%, respectively. In contrast, {101}/{001}-co-faceted TiO_2 demonstrated a slightly lower mass loss of 4.67%. The weight loss below 120 °C was attributed to the elimination of physiosorbed water molecules, while the loss above 120 °C was due to the evaporation of surface-adsorbed hydroxyl groups and the removal of unreacted residues such as F^- and Cl^-, which may account for the increased weight loss in {101} and {001} faceted TiO_2 compared to pure TiO_2. A similar weight loss pattern has been observed in previous studies.[49–51]

Table 5 Calculation of the percentage of {001} and {101} plane in the synthesized TiO_2 samples

Sample	Intensity of the 144 cm^{-1} peak	Intensity of the 514 cm^{-1} peak	Percentage of {001}	Percentage qof {101}
{101}	19 639.96	1094.11	5.57	94.43
{001}	18 162.15	6443.15	35.48	64.52
{101/001}	28 353.15	1446.65	5.10	94.90

Fig. 5 illustrates the surface morphology of the synthesized {101}-faceted (Fig. 5A), {001}-faceted (Fig. 5B) and {101}/{001}-co-faceted (Fig. 5C) TiO_2 samples. A large amount of aggregated nanosheets was observed at both lower and higher magnifications for the {001}-faceted TiO_2. This observation verifies the formation of {001} facets, of a shape similar to those reported in previous literature.[14] In contrast, the {101} faceted TiO_2 particles are densely aggregated and distorted in shape. Although the structure is not clearly understood, previous studies suggest that the shape of this sample could correspond to nanowires. One such particle, appearing as a nanowire, is highlighted in the zoomed-in figure.[52] Similarly, the morphology of the {101}/{001} co-faceted TiO_2 samples was not clearly defined, as both low and high magnification images revealed densely aggregated, distorted, and irregular shapes. The particle sizes of the {101} and {001}-faceted TiO_2 nanoparticles were found to be similar, with average dimensions of 120.106 nm and 80.833 nm, respectively, as analyzed using ImageJ for image processing and Origin for data visualization (Fig. S11). Although these two samples showed no significant size differences, the {101}/{001} co-faceted TiO_2 demonstrated a substantially larger average particle size of 1027.06 nm. This notable increase is likely due to particle aggregation or enhanced growth caused by interactions between the two facets during the synthesis process.

The EDX spectrum analysis for the {101} and {001}-faceted TiO_2 nanoparticles is shown in Fig. S12a and b. The EDX results validate the exclusive presence of titanium (Ti) and oxygen (O) in both samples, with their corresponding peaks in the spectrum at the expected locations. According to the weight percentage analysis, the {101}-faceted TiO_2 contained 30.98% oxygen and 69.02% titanium, while the {001}-faceted TiO_2 showed 30.05% oxygen and 69.95% titanium, reflecting similar

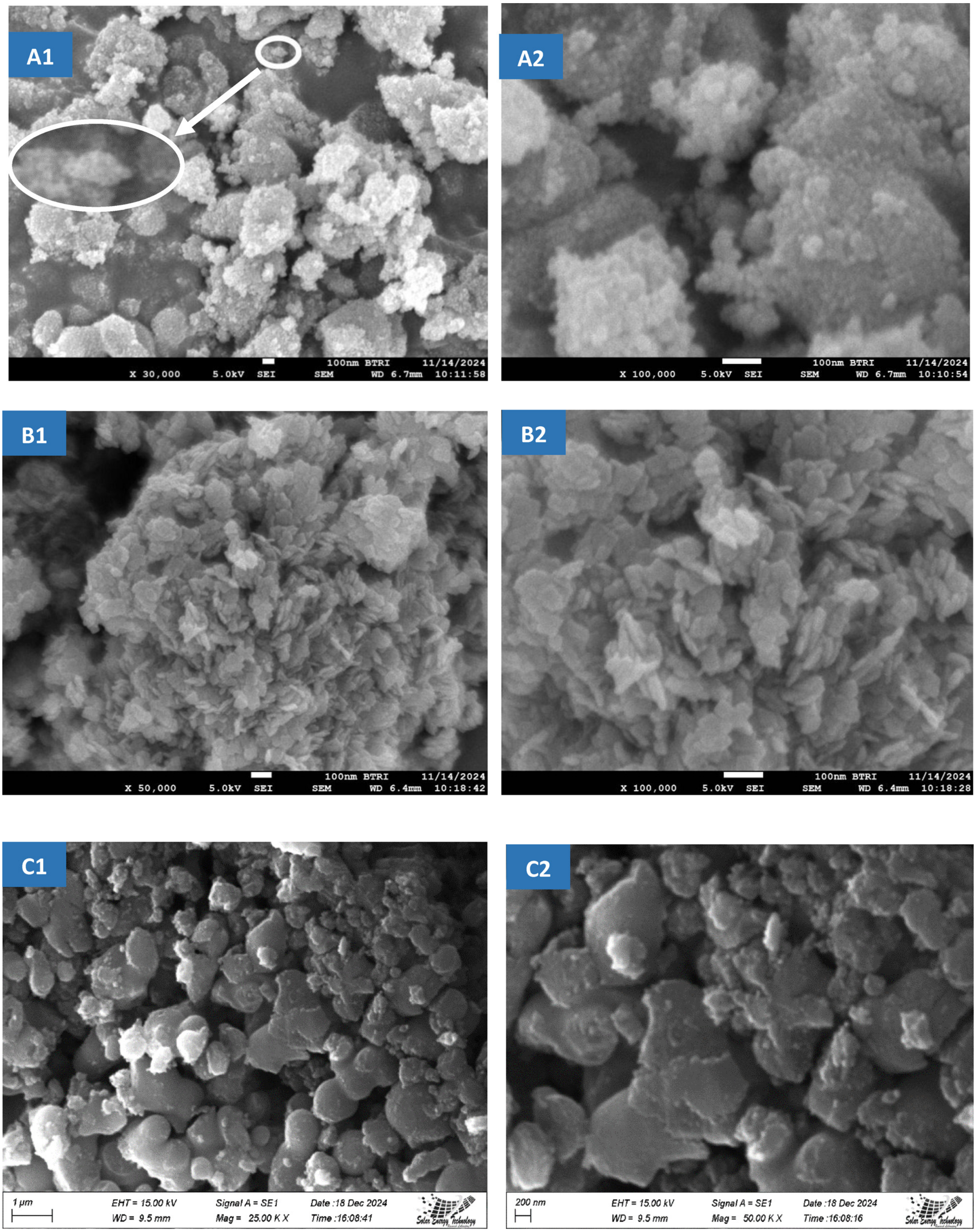

Fig. 5 FESEM image of the synthesized (A) {101}-faceted, (B) {001}-faceted, and (C) {101}/{001} co-faceted TiO_2 samples.

chemical profiles. The results align well with the anticipated compositions, providing evidence of the successful synthesis of the TiO_2 nanoparticles.

Photocatalytic degradation of dye

The photocatalytic performance of the TiO_2 samples was assessed using CR as a model dye over a 30 min period, with the degradation percentages presented in Fig. 6(a). Both {001}-faceted and {101}/{001}-co-faceted TiO_2 samples achieved complete degradation of CR (100%) within the allotted time, while the {101}-faceted TiO_2 demonstrated a lower degradation efficiency of 69.36%. The enhanced photocatalytic activity of the {001}-faceted and {101}/{001}-co-faceted TiO_2 can be attributed to the superior surface reactivity and larger surface area of the {001} facet.[53]

Fig. 6(b) illustrates the degradation percentages obtained from the scavenging tests using IPA and EDTA. In the presence of isopropanol (IPA), an $^{\bullet}OH$ radical quencher, the degradation efficiency of {001}- and {101}/{001}-faceted TiO_2 decreased sharply from 100% to 12.7% and 49.88%, respectively, confirming that $^{\bullet}OH$ radicals are the dominant oxidative species generated on the {001} surface. Likewise, addition of EDTA, a hole (h^+) scavenger, reduced the degradation efficiency of {001} and {101}/{001} TiO_2 to 28.81% and 20.33%, respectively.

The reusability of the photocatalysts was evaluated over five consecutive degradation cycles, as shown in Fig. 6(c). The {101}-faceted TiO_2 exhibited the best performance with 79.90% degradation efficiency even after the fifth cycle, while the {001}-faceted TiO_2 maintained 55.84%. In contrast, the {101}/{001}-co-faceted TiO_2 initially showed the highest degradation efficiency during the first four cycles, with nearly comparable performance in each run; however, its activity declined in the last few cycles, reaching only 42.69% degradation efficiency.

Fig. 6(d) depicts the kinetics of CR dye degradation over the synthesized TiO_2 samples, fitted using the Langmuir–Hinshelwood model according to the equation:[54,55]

$$\ln(C_0/C_t) = K_{\mathrm{app}}t$$

where C_0 and C_t are the initial and time-dependent concentrations, respectively, and K_{app} is the apparent first-order rate constant. A linear relationship was obtained by plotting $\ln(C_0/C_t)$ *versus* irradiation time (t), and the slope corresponds to K_{app}. The calculated rate constants (visualized in Fig. 6(d)) were 0.0202 min^{-1} for {101}-faceted TiO_2, 0.0081 min^{-1} for {001}-faceted TiO_2, and 0.0127 min^{-1} for {101}/{001}-co-faceted TiO_2.

Antimicrobial activity

The antimicrobial activity of the synthesized TiO_2 samples, including {101}-faceted TiO_2 (T1), {001}-faceted TiO_2 (T2), and {101}/{001}-cofaceted TiO_2 (T3), was assessed against two Gram-positive bacteria, two Gram-negative bacteria, and a fungal strain. Chloramphenicol served as the positive control for antibacterial activity, while Azoxystrobin was used as the positive control for antifungal activity.

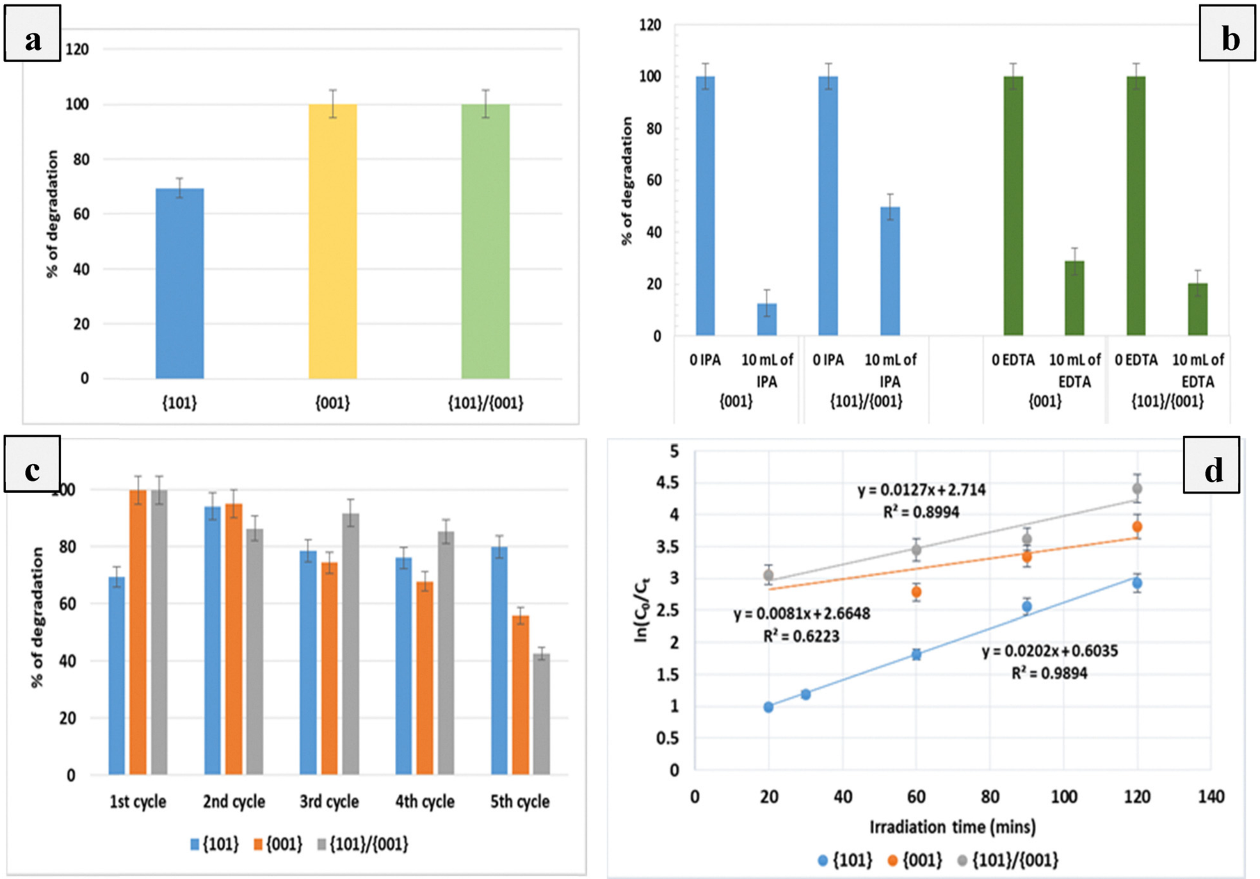

Fig. 6 (a) CR degradation percentage, (b) scavenging analysis, (c) reusability, and (d) kinetics of the photocatalytic degradation of the synthesized TiO_2 samples.

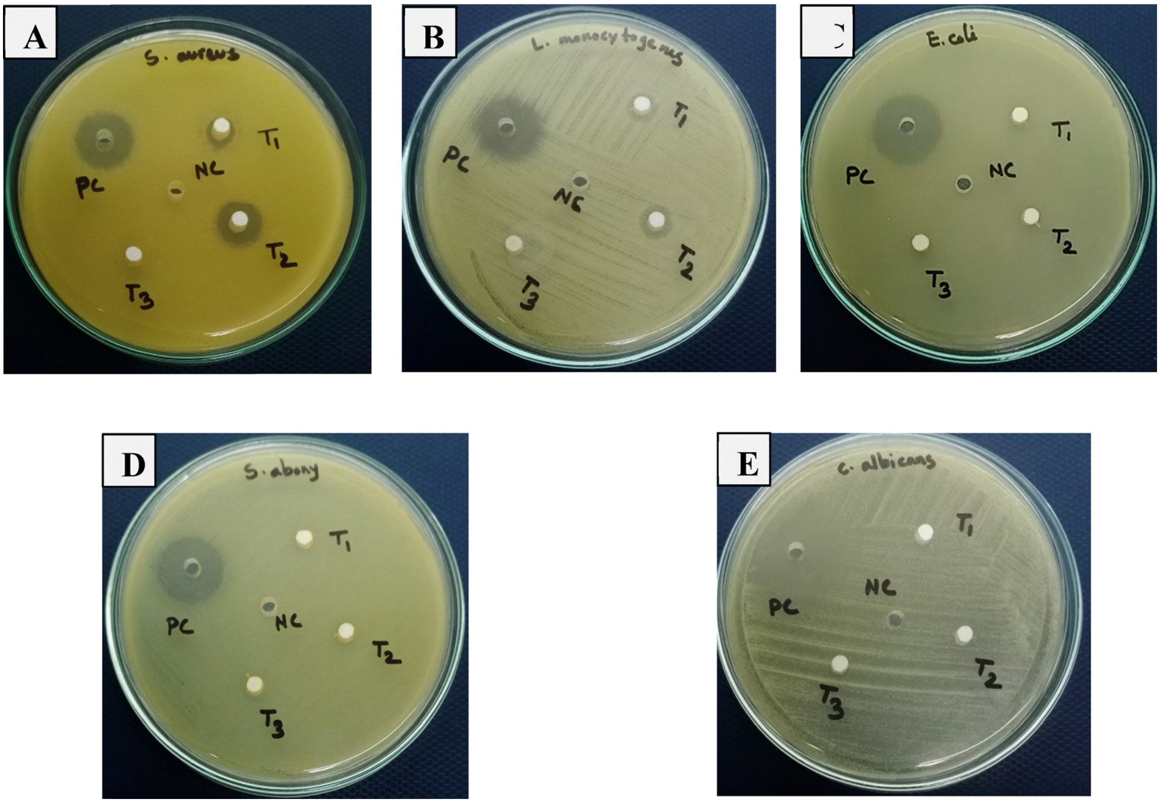

Fig. 7 Evaluation of antimicrobial properties of the synthesized TiO_2 samples against (A) *S. aureus*, (B) *L. monocytogenes*, (C) *E. coli*, (D) *S. abony*, and (E) *C. albicans*.

As shown in the results (Fig. 7), both {101} and {001}-faceted TiO_2 demonstrated notable antimicrobial activity against Gram-positive bacteria but exhibited inadequate activity against Gram-negative bacteria and the fungal strain, with inhibition zones falling below the detection limit of 6 mm. Among the tested samples, {001}-faceted TiO_2 (T2) exhibited the highest antibacterial activity against *L. monocytogenes*, with an inhibition zone of 11.5 ± 0.50 mm, followed by comparable activity against *S. aureus* (11.5 ± 0.50 mm). In contrast, {101}-faceted TiO_2 (T1) showed slightly lower antibacterial activity, with inhibition zones of 9.2 ± 0.91 mm against *S. aureus* and 8.6 ± 0.40 mm against *L. monocytogenes*. These results suggest that both {101} and {001}-faceted TiO_2 samples possess significant antimicrobial efficacy against Gram-positive bacteria under the tested conditions. However, the {101}/{001} co-faceted TiO_2 (T3) failed to exhibit adequate antimicrobial activity against any of the tested microorganisms. In contrast, the positive controls (Chloramphenicol for bacteria and Azoxystrobin for fungi) displayed excellent antimicrobial activity, confirming the validity of the assay. Table 6 shows the inhibition zone diameters, summarizing the antimicrobial activity of the tested samples against the selected microbes.

Electrochemical analysis

To evaluate the electrochemical performance of the {001}-modified GC electrode, cyclic voltammetry was conducted at the potential range of −0.5 to 1.0 V with a scan rate of 100 mV s^{-1} using 2.5 μM $[Fe(CN)_6]^{3-/4-}$ as a redox probe containing 0.1 M NaCl as the supporting electrolyte, illustrated in Fig. 8(a). The {001}-modified electrode exhibited an anodic peak potential ($E_{p.a}$) of 0.24704 V and a cathodic peak potential ($E_{p.c}$) of 0.10115 V, resulting in a peak-to-peak separation (ΔE) of 145.89 mV. This value was significantly lower than that of the bare GC electrode [$E_{p.a}$ = 0.37406 V, $E_{p.c}$ = 0.08920 V, and ΔE = 284.86 mV]. The reduced ΔE suggests enhanced electron transfer kinetics. A comparable effect has been reported in the literature for the G/PANI nanocomposite-modified electrodes.[56] Moreover, the {001}-modified electrode exhibited a higher anodic peak current ($I_{p.a}$ = 97.28 μA cm^{-2}) and cathodic peak current ($I_{p.c}$ = 53.80 μA cm^{-2}) compared to the bare GC electrode ($I_{p.a}$ = 38.90 μA cm^{-2}, $I_{p.c}$ = 37.01 μA cm^{-2}). This variation in both potential and current can be attributed to the surface modification of the GC electrode, which enhances its electrochemical activity and charge transfer efficiency.

The effect of scan rate is crucial in the sensing process as it provides insight into the nature of mass transport at the interface.[57] To study this, anodic stripping voltammetry (ASV) was conducted within a scan rate range of 10 to 120 mV s^{-1}, using a fixed concentration of 5 ppm Pb^{2+}, as shown in Fig. 8(b). The results show that the peak current increases with the scan rate, while the potential shifts in the positive direction, indicating the irreversibility of the reaction at the electrode surface. A linear relationship ($y = 0.2351x + 0.1506$) with a regression coefficient of 0.8867, obtained from the plot of peak

Table 6 Antimicrobial activity of the synthesized TiO_2 samples

	Name of tested microorganisms, diameter of zone of inhibition (mm)				
	Gram-positive		Gram-negative		Fungus
Sample name	*S. aureus*	*L. monocytogenes*	*E. coli*	*S. abony*	*C. albicans*
{101}-faceted TiO_2	9.2 ± 0.91	8.6 ± 0.40	$<6^a$	$<6^a$	$<6^a$
{001}-faceted TiO_2	11.2 ± 0.76	11.5 ± 0.50	$<6^a$	$<6^a$	$<6^a$
{101}/{001}co-faceted TiO_2	$<6^a$	$<6^a$	$<6^a$	$<6^a$	$<6^a$
Positive control	15.9 ± 2.69	15.2 ± 0.75	17.9 ± 4.25	17.2 ± 0.89	16.3 ± 1.10

[a] <6 mm = no significant antimicrobial activity was observed.

current *versus* the square root of the scan rate (Fig. 8(c)), suggests that the mass transport at the electrode interface is diffusion-controlled.

The effectiveness of the fabricated sensor for detecting Pb^{2+} was assessed using ASV within the concentration range of 1 to 10 ppm, under the experimental conditions of a 160 s deposition time, deposition voltage of −1.2 V, scan range of −0.8 to 0.5 V, and a scan rate of 20 mV s^{-1} (displayed in Fig. 8(d)). ASV works by applying a higher negative potential than the reduction potential, allowing metal ions to deposit on the electrode surface. In this experiment, the reduction potential was found to be around +0.07 V, thus the deposition was performed at −1.2 V, fixed after several variations. A linear relationship ($y = 0.032x + 0.6453$) with a regression coefficient of 0.8519 showed good linearity between 1 and 10 ppm, with peak current increasing linearly with Pb^{2+} concentration (Fig. 8(e)). This behavior stems from the presence of a moiety that reacted actively with the targeted analyzed ions.[58] After deposition, the reduced metals were stripped from the electrode surface within a potential range of −0.8 V to 0.5 V. The limit of detection (LOD) was calculated using the slope and standard deviation (LOD = 3 × SD/slope), yielding a value of 9.378 ppm for Pb^{2+} detection. The limit of quantification (LOQ) was calculated similarly (LOQ = 10 × SD/slope), with the resulting value being 31.262 ppm.

The repeatability of the electrode's response to Pb^{2+} ions was evaluated through multiple ASV experiments at the concentration of 0.01 ppm (shown in Fig. 8(f)). The results show consistent peak current values with no significant variation, confirming its reliability and accuracy in the detection of Pb^{2+} ions.

Discussion

TiO_2 has garnered significant attention as one of the most extensively studied metal oxides, owing to its exceptional surface, electronic, and catalytic properties. These attributes are further enhanced when specific crystal facets are exposed, which influence its reactivity, making it a promising candidate for various applications.[59] In this study, TiO_2 nanoparticles were synthesized with exposed {101}, {001}, and {101}/{001} facets to explore their structural and photocatalytic properties. The successful formation of anatase-phase TiO_2 was confirmed through XRD, FTIR and Raman analysis. Crystallite size calculations using various XRD models revealed that the crystallite sizes of all samples, except LSLM, fall within the range of 0–50 nm.

Growth preference and texture coefficient analyses verified that the synthesized TiO_2 nanoparticles were formed with specific exposed facets. For the {101}-faceted TiO_2, the growth preference was observed on the (004) and (105) planes, reflecting a thermodynamically favored growth direction. However, the texture coefficient for the (004) plane was relatively low, suggesting minimal growth along the {001} direction, confirming that the {101} direction is the dominant exposed facet. On the other hand, {001}-faceted TiO_2 exhibited a positive growth preference value and good texture coefficient for the (004) plane, confirming the dominance of the {001} facet in the sample. The co-faceted samples, which displayed higher texture coefficients for both the (105) and (004) planes, were characterized by the coexistence of both {101} and {001} facets. Raman analysis also confirmed growth on specific facets, as the {101}-faceted sample has 94.43% growth in the {101} direction, whereas the {001}-faceted sample has 35.48% growth in the {001} direction. However, for the {101}/{001} co-faceted sample, Raman analysis indicated growth only along the {101} direction, despite growth preference and texture coefficient analyses confirming the presence of both facets. This discrepancy may be attributed to the sample's morphology, where the particles exhibit significant aggregation, leading to cluster formation and an increase in particle size, as evidenced by the histogram analysis, which recorded a large particle size of 1027.6 nm. The larger particle size causes volume expansion, increasing the vibrational amplitude of neighboring molecules due to a rise in the mean square relative displacement. As a result, the Raman shift increases, particularly for the E_g peaks at 144 cm^{-1}, disrupting the accurate estimation of the {001} facet percentage. A similar pattern is also seen in previous literature.[60]

The morphological features of the synthesized TiO_2 nanoparticles were further examined using FESEM. The {001}-faceted samples displayed a nanosheet-like structure, while the {101}-faceted samples exhibited an aggregated nanowire structure, consistent with previous findings.[14,52] These distinct morphologies are consistent with the crystallographic preferences observed in the XRD and texture coefficient analysis, underscoring the influence of facet engineering on the structural properties of TiO_2 nanoparticles.

TiO_2 nanoparticles have demonstrated versatility in a wide range of applications, including photocatalytic degradation,

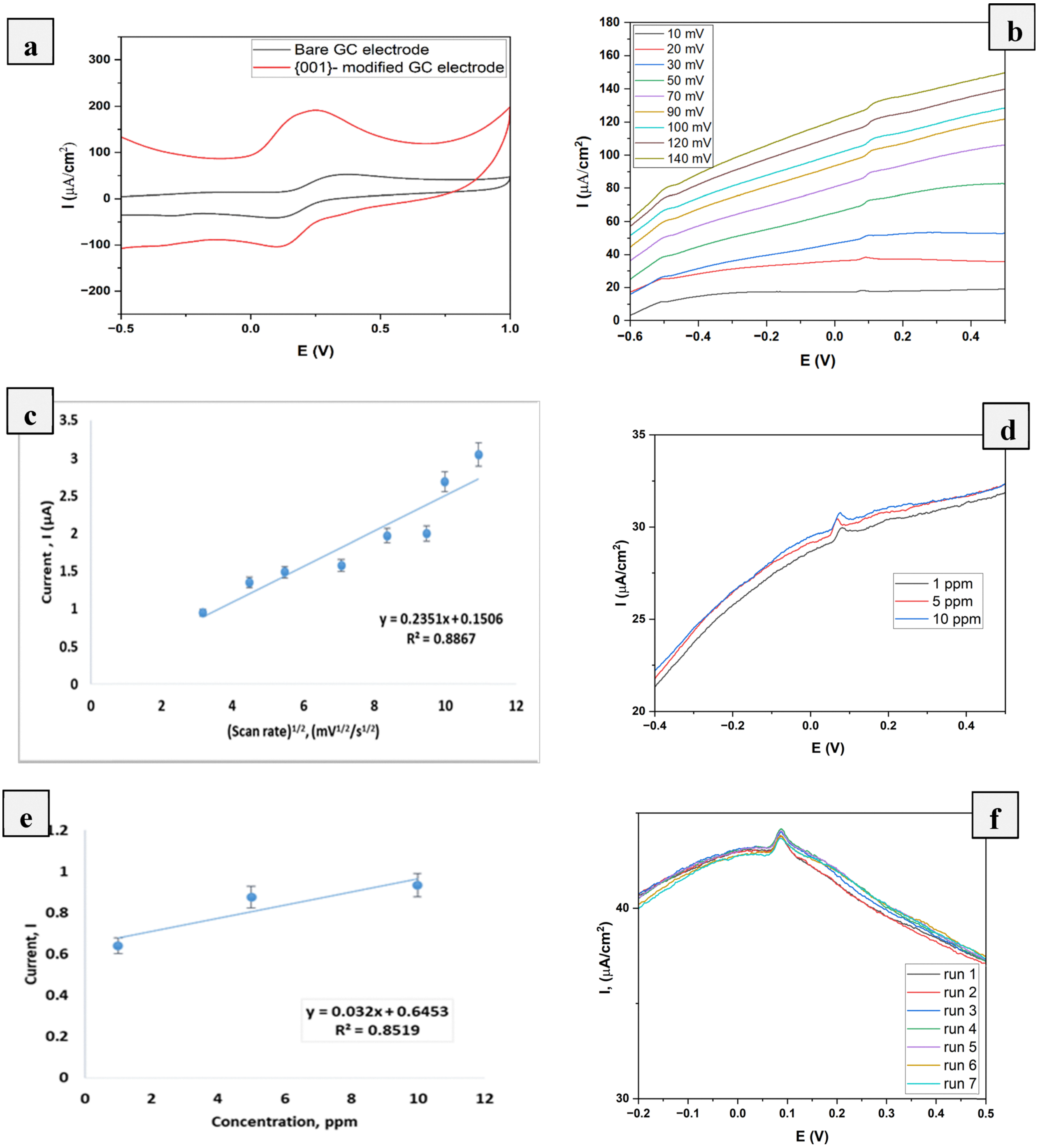

Fig. 8 (a) CV of the bare GC electrode and {001}-faceted TiO_2 modified GC electrode at 2.5 μM $[Fe(CN)_6]^{3-/4-}$. (b) ASV of the {001}-faceted TiO_2 modified GC electrode at different scan rate ranges from 10–140 mV using 5 ppm Pb^{2+} solution. (c) Relationship between the current and square root of the scan rate measured in 5 ppm Pb^{2+} solution. (d) ASV of Pb^{2+} at different concentrations maintaining a scan rate of 20 mV, at a GC modified electrode. (e) Relationship between the current and concentration of Pb^{2+} measured at 20 mV scan rate, 1–10 ppm concentration range. (f) ASV of the repeatability test using 0.01 ppm Pb^{2+} solution multiple times.

sensors, dye-sensitized solar cells, charge-spreading devices, photoluminescence, bactericides, optical coatings, and optoelectronic devices. In this study, the synthesized TiO_2 nanoparticles were utilized for the photocatalytic degradation of CR dye, assessment of antimicrobial activity, and electrochemical sensing for Pb detection.

CR dye is a common pollutant in textile wastewater. The {001}-faceted and {101}/{001}-co-faceted TiO_2 achieved complete degradation of CR dye in just 30 min, compared to 69.36% degradation by {101}-faceted TiO_2 under identical conditions. This superior performance is attributed to the unique properties of the highly exposed {001} facets. The {001} facet is highly reactive due to its higher surface energy compared to the {101} facet. This is a result of the greater density of unsaturated bonds between penta-coordinated Ti (Ti_{5C}) atoms and two-fold coordinated oxygen atoms (O_{2C}).[61] Notably, the {001} facets consist entirely of Ti_{5C} atoms (100%), making them fully accessible for photocatalytic reactions. In contrast, the {101} facet has only 50% Ti_{5C} atoms, which reduces its reactivity.[53] Furthermore, the Ti_{5C}–O_{2C} bonds on the {001} facet have a larger bond length (1.95 Å), making them easier to break upon reactant adsorption. This enhances the activity of titanium and oxygen atoms on the {001} surface, promoting photocatalytic reactions.[62] Furthermore, these attributes enhance the generation of reactive oxygen species (ROS) that attack dye molecules at or near the photocatalyst surface and are mainly responsible for the degradation. In particular, the {001} facets have been shown to facilitate $^{\bullet}OH$ radical formation owing to their lower activation energy for $^{\bullet}OH$ generation.[63] This was confirmed by scavenging experiments: in the presence of isopropanol (IPA), an $^{\bullet}OH$ radical quencher, the degradation efficiency of {001}-faceted TiO_2 dropped dramatically from 100% to 12.7%, indicating that $^{\bullet}OH$ radicals are the dominant oxidative species. In contrast, the addition of EDTA reduced the degradation efficiency of {001} and {101}/{001} TiO_2 to 28.81% and 20.33%, respectively. These results demonstrate that $^{\bullet}OH$ radicals play the primary role in the photocatalytic process over {001}-faceted TiO_2, while photogenerated holes also make a significant contribution. Overall, these findings establish that the {001} facet is highly effective in facilitating ROS generation, thereby accelerating CR dye degradation.

Previous studies have also demonstrated that facet-engineered TiO_2 exhibits enhanced photocatalytic activity compared to pure or commercial TiO_2. For instance, Hammud *et al.* reported that commercial P25 (Degussa) TiO_2 achieved only 60–90% Congo Red degradation after 60 min of UV irradiation at different catalyst dosages.[64] Lee *et al.* investigated the photocatalytic degradation of methylene blue using {101}/{001}-faceted TiO_2 and observed a higher activity with an apparent rate constant of 0.0527 min^{-1}.[65] Roy *et al.* synthesized TiO_2 *via* a green approach using amines and found that samples with ∼25% {101} and ∼75% {100}/{010} exposed facets exhibited 3.7 and 3.1-fold higher photocatalytic activity than Degussa P25 toward methyl orange and methylene blue, respectively.[66] Similarly, Leu *et al.* demonstrated that {001}-exposed TiO_2 composites showed significantly higher photocatalytic activity for methylene blue degradation under both UV and visible light irradiation,[67] while Gul *et al.* reported that highly {001}-faceted TiO_2 exhibited superior degradation of crystal violet and methyl orange compared to pure TiO_2.[68] In another study, John *et al.* employed *C. odorata* leaf extract for the green synthesis of N-doped {001}-faceted TiO_2, achieving ∼98% degradation of methylene blue.[69] Likewise, Kaur *et al.* synthesized *E. cardamomum*-wrapped TiO_2, where phytochemicals in the extract preferentially stabilized the {100} facets, resulting in 97% Congo Red degradation within 150 min.[70] Collectively, these findings confirm that {001}-exposed TiO_2 nanoparticles, particularly those synthesized through green or modified routes, can outperform commercial P25 and represent promising candidates for advanced oxidation processes aimed at degrading persistent pollutants and improving water quality.

In addition to photocatalytic degradation, {001}-faceted TiO_2 exhibited strong antimicrobial properties against Gram-positive bacteria, with inhibition zones of 11.5 ± 0.50 mm against *L. monocytogenes* and 11.5 ± 0.50 mm against *S. aureus*. In comparison, {101}-faceted TiO_2 showed inhibition zones of 9.2 ± 0.91 mm against *S. aureus* and 8.6 ± 0.40 mm against *L. monocytogenes*. This enhanced antibacterial activity of {001}-faceted TiO_2 is attributed to its greater reactivity, primarily due to the presence of unsaturated coordinated Ti atoms on the surface. These unsaturated Ti atoms interact readily with bacterial cell membranes, leading to membrane disruption. This disruption triggers oxidative stress, causing leakage of intracellular contents and ultimately resulting in bacterial cell death.[40] {001} Facets have 100% unsaturated coordinated Ti atoms, while {101} facets have only 50%, which accounts for the superior antimicrobial properties of {001}-faceted TiO_2. In contrast, the poor antimicrobial activity against Gram-negative bacteria may be due to the presence of an additional outer membrane, unlike Gram-positive bacteria, and a plasma membrane composed of both anionic and zwitterionic phospholipids, which reduces nanoparticle interaction and penetration.[71] Similarly, *C. albicans* exhibits limited susceptibility because, as a eukaryotic organism, it has a thick cell wall and a complex, sugar-rich cell membrane that act as a protective barrier against nanoparticle entry.[72]

The electrochemical properties of the {001}-modified TiO_2 electrode were also evaluated for Pb^{2+} ion detection through the fabrication of an electrochemical sensor using {001}-faceted TiO_2. CV confirmed that the modified electrode exhibited superior electrochemical efficiency compared to the bare GC electrode, as evidenced by reduced potential difference and enhanced current response, indicating improved charge transfer efficiency. ASV was employed to assess the mass transport mechanism at the electrode interface, revealing that the Pb^{2+} detection process was governed by an irreversible, diffusion-controlled reaction. The fabricated sensor demonstrated a LOD of 9.378 ppm and a LOQ of 31.162 ppm, confirming its sensitivity for Pb^{2+} detection. Table 7 shows the comparison of the electrochemical sensing performance for Pb^{2+} between the fabricated sensor and previous studies. Although the bare GC electrode showed significant improvement and detectable sensitivity toward Pb^{2+} with {001}-faceted modification, the LOD and LOQ can be further enhanced using nanocomposite-based electrodes or surface functionalization. Incorporating conductive nanomaterials (graphene,[73] carbon nanotubes[74]), metallic nanoparticles (Bi,[75] Au[76]), or MXene-[77] and MOF/COF-based[78] hybrid modifiers can substantially increase the active surface area, accelerate electron transfer, and enable effective preconcentration. For example, Zhang *et al.*'s MWCNT/MOF (ZIF-67)-modified GCE exhibited excellent conductivity and a high density of binding sites, achieving a LOD as low as 1 nM and an extended linear range of 1.38 nM–5 μM.[78] Surface functionalization with thiol or carboxyl groups can further

Table 7 Comparison of electrochemical sensing performance for Pb^{2+} between the fabricated sensor and previous studies

Material	Method	Linear range	Limit of detection, LOD	Limit of quantification, LOQ	Ref.
Biomass-worm like nitrogen doped-carbon	DPASV	0.5–100 mg L^{-1}	0.2 mg L^{-1}	—	81
TiO_2@Gum Arabic	DPV	1–10 ppm	0.56 ppm	1.68 ppm	82
MOF/EB-1	Voltammetry	0.54–1.15 ppm	0.077 ppm	—	83
BC@TiO_2NPs	DPV	1×10^{-6}–10 µM	0.6268×10^{-6} µM	—	84
Ti/TiO_2	ASV	0.6–13.2 µM	140 nM	—	85
TiO_2/AgCNF	SWASV	—	40.14 nM	—	86
$NiWO_4$/MWCNT	DPV	50–450 µM	0.12 µM		87
TiON/TiO_2	SWASV	10^{-5}–10^{-1} mol L^{-1}	10^{-5} mol L^{-1}	1.0 × 10–4 mol L^{-1}	88
{001}-faceted TiO_2	LSASV	(1–10) ppm	9.378 ppm	31.162 ppm	This study

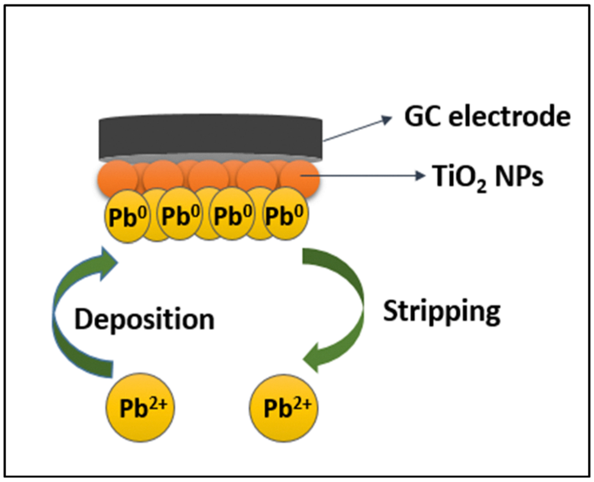

Fig. 9 Sensing mechanism of the {001}-modified TiO_2 sensor for Pb^{2+} ion detection.

improve selectivity for Pb^{2+} ions. For instance, Oliveira *et al.* reported ZnO nanofibers functionalized with L-cysteine for Pb^{2+} electrochemical sensing, achieving a LOD of 0.397 µg L^{-1} within a linear range of 10–140 µg L^{-1}.[79] Fig. 9 illustrates the sensing mechanism for Pb^{2+} ion detection using the fabricated sensor. Upon applying a deposition voltage of −1.2 V, Pb^{2+} ions adsorbed onto the surface of the modified electrode and are reduced to Pb^0. A subsequent stripping potential between −0.8 V and 0.5 V reoxidized Pb^0 back to Pb^{2+}, leading to desorption from the electrode.[80] The enhanced sensing capability of the {001}-modified TiO_2 electrode can be attributed to its high surface reactivity, which enables efficient interaction with Pb^{2+} ions. The repeatability tests further confirmed the electrode's stability and accuracy, demonstrating consistent peak current responses for multiple measurements.

Conclusion

In this study, anatase-phase TiO_2 nanoparticles with exposed {101}, {001}, and {101}/{001} facets were successfully synthesized using inorganic modifiers *via* a hydrothermal method. The photocatalytic degradation of CR dye under visible light irradiation demonstrated that {001}-faceted and {101}/{001} co-faceted TiO_2 exhibited complete degradation within 30 min, significantly outperforming {101}-faceted TiO_2. This underscores the critical role of facet engineering in optimizing TiO_2 for environmental remediation applications. Furthermore, the antimicrobial studies revealed that {001}-faceted TiO_2 demonstrated superior antibacterial efficacy against Gram-positive bacteria compared to {101}-faceted TiO_2. Moreover, {001}-faceted TiO_2 exhibited excellent electrochemical performance for Pb^{2+} ion detection, with a higher electroactive surface area of the fabricated sensor, facilitating efficient charge transfer and enhancing sensor performance. The sensor demonstrated a LOD of 9.378 ppm and a LOQ of 31.162 ppm. Overall, the findings demonstrate that {001}-faceted TiO_2 holds great promise for multifunctional applications, including environmental pollutant degradation, antibacterial treatments, and electrochemical sensing. Future research should aim to further improve sensitivity and selectivity through the incorporation of conductive nanomaterials, metal nanoparticles, or surface functionalization with thiol/carboxyl groups. Additionally, extending the work to real wastewater samples and other emerging contaminants, such as pharmaceutical residues, will strengthen the practical applicability of these materials.

Author contributions

Md. Anayet Ullah: curated and analyzed the data; wrote the manuscript. Newaz Mohammed Bahadur: visualized the whole research. Dipa Islam, Subarna Shandani dey, and Md. Farhad Ali: helped in data curation. Fataha Nur Robel and Samina Ahmed: supervised the findings of this work. Md. Sahadat Hossain: conceived and designed the study; analyzed the data; supervised the overall work and reviewed the manuscript.

Conflicts of interest

There are no conflicts to declare.

Data availability

Data will be made available on request.

The data supporting this article have been included as part of the supplementary information (SI). Supplementary information is available. See DOI: https://doi.org/10.1039/d5ma00760g.

Acknowledgements

The Bangladesh Council of Scientific and Industrial Research (BCSIR) is acknowledged by the authors for its financial support of research and development projects (ref. no. 39.02.0000.011.14.180.2024/1116; Date: 14.01.2025). Additionally, Md. Anayet Ullah expresses gratitude to Noakhali Science and Technology University's Department of Applied Chemistry and Chemical Engineering for supporting his MS thesis program at Noakhali, Bangladesh.

References

1 J. Sun, *et al.*, Synthesis of anatase TiO_2 with exposed {001} and {101} facets and photocatalytic activity, *Rare Met.*, 2019, **38**(4), 287–291, DOI: 10.1007/s12598-014-0329-9.

2 B. O'Regan and M. Grätzel, A low-cost, high-efficiency solar cell based on dye-sensitized colloidal TiO_2 films, *Nature*, 1991, **353**(6346), 737–740, DOI: 10.1038/353737a0.

3 M. Khairy and W. Zakaria, Effect of metal-doping of TiO_2 nanoparticles on their photocatalytic activities toward removal of organic dyes, *Egypt. J. Pet.*, 2014, **23**(4), 419–426, DOI: 10.1016/j.ejpe.2014.09.010.

4 C. Zhou, S. Hong, X. Chen, Q. Li, Z. Chen and S. Yang, Screen-Assisted Self-Spreading of TiO_2 Precursor Solution on FTO Substrates for High-Quality Electron Transport Layers in Perovskite Solar Cells, *ACS Appl. Mater. Interfaces*, 2024, **16**(34), 45020–45029, DOI: 10.1021/acsami.4c10820.

5 X. Tian, *et al.*, Gas sensors based on TiO_2 nanostructured materials for the detection of hazardous gases: a review, *Nano Mater. Sci.*, 2021, **3**(4), 390–403, DOI: 10.1016/j.nanoms.2021.05.011.

6 W. F. Zhang, M. S. Zhang and Z. Yin, Microstructures and Visible Photoluminescence of TiO_2 Nanocrystals, *Phys. Status Solidi A*, 2000, **179**(2), 319–327, DOI: 10.1002/1521-396X(200006)179:2<319::AID-PSSA319>3.0.CO;2-H.

7 H. M. Yadav, *et al.*, Preparation and characterization of copper-doped anatase TiO_2 nanoparticles with visible light photocatalytic antibacterial activity, *J. Photochem. Photobiol., A*, 2014, **280**, 32–38Available: https://www.sciencedirect.com/science/article/abs/pii/S1010603014000471.

8 C. Euvananont, C. Junin, K. Inpor, P. Limthongkul and C. Thanachayanont, TiO_2 optical coating layers for self-cleaning applications, *Ceram. Int.*, 2008, **34**(4), 1067–1071, DOI: 10.1016/j.ceramint.2007.09.043.

9 B. Sathyaseelan, *et al.*, Structural, optical and morphological properties of post-growth calcined TiO_2 nanopowder for opto-electronic device application: *ex situ* studies, *J. Alloys Compd.*, 2016, **671**, 486–492, DOI: 10.1016/j.jallcom.2016.02.105.

10 T. Berger, D. Monllor-Satoca, M. Jankulovska, T. Lana-Villarreal and R. Gómez, The Electrochemistry of Nanostructured Titanium Dioxide Electrodes, *ChemPhysChem*, 2012, **13**(12), 2824–2875, DOI: 10.1002/cphc.201200073.

11 M. Radetić, Functionalization of textile materials with TiO_2 nanoparticles, *J. Photochem. Photobiol., C*, 2013, **16**, 62–76, DOI: 10.1016/j.jphotochemrev.2013.04.002.

12 G. V. Khade, M. B. Suwarnkar, N. L. Gavade and K. M. Garadkar, Green synthesis of TiO_2 and its photocatalytic activity, *J. Mater. Sci.: Mater. Electron.*, 2015, **26**(5), 3309–3315, DOI: 10.1007/s10854-015-2832-7.

13 U. Diebold, The surface science of titanium dioxide, *Surf. Sci. Rep.*, 2003, **48**(5–8), 53–229, DOI: 10.1016/S0167-5729(02)00100-0.

14 M. Chen, *et al.*, Remarkable synergistic effect between {001} facets and surface F ions promoting hole migration on anatase TiO_2, *Appl. Catal., B*, 2017, **207**, 397–403, DOI: 10.1016/j.apcatb.2017.02.048.

15 Z. Xiong, Z. Lei, Y. Li, L. Dong, Y. Zhao and J. Zhang, A review on modification of facet-engineered TiO_2 for photocatalytic CO_2 reduction, *J. Photochem. Photobiol., C*, 2018, **36**, 24–47, DOI: 10.1016/j.jphotochemrev.2018.07.002.

16 H. Irie, S. Washizuka and K. Hashimoto, Hydrophilicity on carbon-doped TiO_2 thin films under visible light, *Thin Solid Films*, 2006, **510**(1–2), 21–25, DOI: 10.1016/j.tsf.2005.08.374.

17 L. Kavan and M. Grätzel, Highly efficient semiconducting TiO_2 photoelectrodes prepared by aerosol pyrolysis, *Electrochim. Acta*, 1995, **40**(5), 643–652, DOI: 10.1016/0013-4686(95)90400-W.

18 A. Monoy, *et al.*, Surface preparation influence on the initial stages of MOCVD growth of TiO_2 thin films, *Thin Solid Films*, 2006, **515**(2), 687–690, DOI: 10.1016/j.tsf.2005.12.237.

19 Y. Lei, L. D. Zhang and J. C. Fan, Fabrication, characterization and Raman study of TiO_2 nanowire arrays prepared by anodic oxidative hydrolysis of $TiCl_3$, *Chem. Phys. Lett.*, 2001, **338**(4–6), 231–236, DOI: 10.1016/S0009-2614(01)00263-9.

20 I. Oja, A. Mere, M. Krunks, R. Nisumaa, C.-H. Solterbeck and M. Es-Souni, Structural and electrical characterization of TiO_2 films grown by spray pyrolysis, *Thin Solid Films*, 2006, **515**(2), 674–677, DOI: 10.1016/j.tsf.2005.12.243.

21 H. Liu, *et al.*, Synthesis and Characterization of Titania Prepared by Using a Photoassisted Sol—Gel Method, *Langmuir*, 2003, **19**(7), 3001–3005, DOI: 10.1021/la026600o.

22 X. Zhao, M. Liu and Y. Zhu, Fabrication of porous TiO_2 film via hydrothermal method and its photocatalytic performances, *Thin Solid Films*, 2007, **515**(18), 7127–7134, DOI: 10.1016/j.tsf.2007.03.025.

23 P. Soundarrajan, K. Sankarasubramanian, K. Sethuraman and K. Ramamurthi, Controlled (110) and (101) crystallographic plane growth of single crystalline rutile TiO_2 nanorods by facile low cost chemical methods, *CrystEngComm*, 2014, **16**(37), 8756–8768, Available: https://pubs.rsc.org/en/content/articlehtml/2014/ce/c4ce00820k.

24 A. Haghighat Mamaghani, F. Haghighat and C.-S. Lee, Hydrothermal/solvothermal synthesis and treatment of TiO_2 for photocatalytic degradation of air pollutants:

Preparation, characterization, properties, and performance, *Chemosphere*, 2019, **219**, 804–825, DOI: 10.1016/j.chemosphere.2018.12.029.

25 D. Majumder and S. Roy, Non-fluorinated synthesis of anatase TiO_2 with dominant {001} facets: influence of faceted structures on formaldehyde sensitivity, *New J. Chem.*, 2017, **41**(15), 7591–7597, Available: https://pubs.rsc.org/en/content/articlehtml/2017/nj/c7nj00648a.

26 H. Liu, S. Liu, Z. Zhang, X. Dong and T. Liu, Hydrothermal etching fabrication of TiO_2@graphene hollow structures: mutually independent exposed {001} and {101} facets nanocrystals and its synergistic photocaltalytic effects, *Sci. Rep.*, 2016, **6**(1), 33839, DOI: 10.1038/srep33839.

27 A. Haleem, *et al.*, In-Depth Photocatalytic Degradation Mechanism of the Extensively Used Dyes Malachite Green, Methylene Blue, Congo Red, and Rhodamine B via Covalent Organic Framework-Based Photocatalysts, *Water*, 2024, **16**(11), 1588, DOI: 10.3390/w16111588.

28 G. E. Quintanilla-Villanueva, A. Sicardi-Segade, D. Luna-Moreno, R. E. Núñez-Salas, J. F. Villarreal-Chiu and M. M. Rodríguez-Delgado, Recent Advances in Congo Red Degradation by TiO_2-Based Photocatalysts Under Visible Light, *Catalysts*, 2025, **15**(1), 84, DOI: 10.3390/catal15010084.

29 L. Ye, J. Mao, J. Liu, Z. Jiang, T. Peng and L. Zan, Synthesis of anatase TiO_2 nanocrystals with {101}, {001} or {010} single facets of 90% level exposure and liquid-phase photocatalytic reduction and oxidation activity orders, *J. Mater. Chem. A*, 2013, **1**(35), 10532–10537, DOI: 10.1039/C3TA11791J.

30 J. Liao, F. Yang, C.-Z. Wang and S. Lin, The crystal facet-dependent electrochemical performance of TiO_2 nanocrystals for heavy metal detection: theoretical prediction and experimental proof, *Sens. Actuators, B*, 2018, **271**, 195–202, DOI: 10.1016/j.snb.2018.05.067.

31 G. Yu, *et al.*, Applications of Nanomaterials for Heavy Metal Removal from Water and Soil: A Review, *Sustainability*, 2021, **13**(2), 713, DOI: 10.3390/su13020713.

32 S. Tajik, *et al.*, Recent Developments in Polymer Nanocomposite-Based Electrochemical Sensors for Detecting Environmental Pollutants, *Ind. Eng. Chem. Res.*, 2021, **60**(3), 1112–1136, DOI: 10.1021/acs.iecr.0c04952.

33 M. Behbahani, N. A. G. Tapeh, M. Mahyari, A. R. Pourali, B. G. Amin and A. Shaabani, Monitoring of trace amounts of heavy metals in different food and water samples by flame atomic absorption spectrophotometer after preconcentration by amine-functionalized graphene nanosheet, *Environ. Monit. Assess.*, 2014, **186**(11), 7245–7257, DOI: 10.1007/s10661-014-3924-1.

34 V. L. Dressler, D. Pozebon and A. J. Curtius, Determination of heavy metals by inductively coupled plasma mass spectrometry after on-line separation and preconcentration, *Spectrochim. Acta, Part B*, 1998, **53**(11), 1527–1539, DOI: 10.1016/S0584-8547(98)00180-3.

35 L. A. Hutton, G. D. O'Neil, T. L. Read, Z. J. Ayres, M. E. Newton and J. V. Macpherson, Electrochemical X-ray Fluorescence Spectroscopy for Trace Heavy Metal Analysis: Enhancing X-ray Fluorescence Detection Capabilities by Four Orders of Magnitude, *Anal. Chem.*, 2014, **86**(9), 4566–4572, DOI: 10.1021/ac500608d.

36 A. Fan, Y. Ling, C. Lau and J. Lu, Direct colorimetric visualization of mercury (Hg^{2+}) based on the formation of gold nanoparticles, *Talanta*, 2010, **82**(2), 687–692, DOI: 10.1016/j.talanta.2010.05.033.

37 S. Li, *et al.*, Electrochemical microfluidics techniques for heavy metal ion detection, *Analyst*, 2018, **143**(18), 4230–4246, DOI: 10.1039/C8AN01067F.

38 C. Ariño, C. E. Banks and A. Bobrowski, Electrochemical stripping analysis, *Nat. Rev. Methods Primers*, 2022, **2**, 62, DOI: 10.1038/s43586-022-00143-5.

39 A. J. Borrill, N. E. Reily and J. V. Macpherson, Addressing the practicalities of anodic stripping voltammetry for heavy metal detection: a tutorial review, *Analyst*, 2019, **144**(23), 6834–6849, DOI: 10.1039/C9AN01437C.

40 V. Stanić and S. B. Tanasković, Antibacterial activity of metal oxide nanoparticles, *Nanotoxicity*, Elsevier, 2020, pp. 241–274, DOI: 10.1016/B978-0-12-819943-5.00011-7.

41 H. Kaur, S. Kumar, R. Saini, P. P. Singh and A. Pugazhendhi, One-pot biogenic synthesis of *C. limon*/TiO_2 with dual applications as an advance photocatalyst and antimicrobial agent, *Chemosphere*, 2023, **335**, 139106, DOI: 10.1016/j.chemosphere.2023.139106.

42 H. Kaur, J. Singh, P. Rani, N. Kaur, S. Kumar and M. Rawat, A novel and one-pot synthesis of *Punica granatum* mediated copper oxide having flower-like morphology as an efficient visible-light driven photocatalyst for degradation of textile dyes in waste water, *J. Mol. Liq.*, 2022, **355**, 118966, DOI: 10.1016/j.molliq.2022.118966.

43 Ms. K. Alam, Md. S. Hossain, N. M. Bahadur and S. Ahmed, A comparative study in estimating of crystallite sizes of synthesized and natural hydroxyapatites using Scherrer Method, Williamson–Hall model, Size-Strain Plot and Halder–Wagner Method, *J. Mol. Struct.*, 2024, **1306**, 137820, DOI: 10.1016/j.molstruc.2024.137820.

44 M. Alam, M. Sahadat Hossain, Md. A. Ullah, N. Bahadur and S. Ahmed, Utilization of marine snails for the sustainable synthesis and crystallographic characterization of nanocrystallite hydroxyapatite, *Hybrid Adv.*, 2024, **7**, 100308, DOI: 10.1016/j.hybadv.2024.100308.

45 M. Rashidzadeh, Synthesis of High-Thermal Stable Titanium Dioxide Nanoparticles, *Int. J. Photoenergy*, 2008, **2008**(1), 245981, DOI: 10.1155/2008/245981.

46 A. León, *et al.*, FTIR and Raman Characterization of TiO_2 Nanoparticles Coated with Polyethylene Glycol as Carrier for 2-Methoxyestradiol, *Appl. Sci.*, 2017, **7**(1), 49, DOI: 10.3390/app7010049.

47 Y. Yang, *et al.*, Surface modification of (001) facets dominated TiO_2 with ozone for adsorption and photocatalytic degradation of gaseous toluene, *Chin. J. Chem. Phys.*, 2019, **32**(5), 611–619, DOI: 10.1063/1674-0068/cjcp1903062.

48 F. Tian, Y. Zhang, J. Zhang and C. Pan, Raman Spectroscopy: A New Approach to Measure the Percentage of Anatase TiO_2 Exposed (001) Facets, *J. Phys. Chem. C*, 2012, **116**(13), 7515–7519, DOI: 10.1021/jp301256h.

49 T. Xu, H. Zheng, P. Zhang, W. Lin and Y. Sekiguchi, Hydrothermal preparation of nanoporous TiO_2 films with exposed {001} facets and superior photocatalytic activity, *J. Mater. Chem. A*, 2015, **3**(37), 19115–19122, DOI: 10.1039/C5TA02640G.

50 G. Jeantelot, Control and Characterization of Titanium Dioxide Morphology: Applications in Surface Organometallic Chemistry, *KAUST Research Repository*, 2014, DOI: 10.25781/KAUST-AVMKW.

51 M. V. Sofianou, *et al.*, Tuning the photocatalytic selectivity of TiO_2 anatase nanoplates by altering the exposed crystal facets content, *Appl. Catal., B*, 2013, **142–143**, 761–768, DOI: 10.1016/j.apcatb.2013.06.009.

52 Y. Zhou, *et al.*, Enhanced dye-sensitized solar cells performance using anatase TiO_2 mesocrystals with the Wulff construction of nearly 100% exposed {101} facets as effective light scattering layer, *Dalton Trans.*, 2014, **43**(12), 4711–4719, DOI: 10.1039/C3DT53010H.

53 L. Ye, J. Mao, J. Liu, Z. Jiang, T. Peng and L. Zan, Synthesis of anatase TiO_2 nanocrystals with {101}, {001} or {010} single facets of 90% level exposure and liquid-phase photocatalytic reduction and oxidation activity orders, *J. Mater. Chem. A*, 2013, **1**(35), 10532–10537, DOI: 10.1039/C3TA11791J.

54 E. Kusvuran, A. Samil, O. M. Atanur and O. Erbatur, Photocatalytic degradation kinetics of di- and tri-substituted phenolic compounds in aqueous solution by TiO_2/UV, *Appl. Catal., B*, 2005, **58**(3), 211–216, DOI: 10.1016/j.apcatb.2004.11.023.

55 V. Goyal, A. Singh, J. Singh, H. Kaur, S. Kumar and M. Rawat, Biogenically structural and morphological engineering of rigonella foenum-graecum mediated SnO_2 nanoparticles with enhanced photocatalytic and antimicrobial activities, *Mater. Chem. Phys.*, 2022, **282**, 125946, DOI: 10.1016/j.matchemphys.2022.125946.

56 N. Ruecha, N. Rodthongkum, D. M. Cate, J. Volckens, O. Chailapakul and C. S. Henry, Sensitive electrochemical sensor using a graphene–polyaniline nanocomposite for simultaneous detection of Zn(II), Cd(II), and Pb(II), *Anal. Chim. Acta*, 2015, **874**, 40–48, DOI: 10.1016/j.aca.2015.02.064.

57 A. Hosseini, E. Sohouli, M. Gholami, A. Sobhani-Nasab and S. A. Mirhosseini, Electrochemical Determination of Ciprofloxacin Using Glassy Carbon Electrode Modified with CoFe2O4-MWCNT, *Anal. Bioanal. Electrochem.*, 2019, **11**(8), 996–1008.

58 R. Kaur, S. Rana, R. Singh, V. Kaur and P. Narula, A Schiff base modified graphene oxide film for anodic stripping voltammetric determination of arsenite, *Microchim. Acta*, 2019, **186**(11), 741, DOI: 10.1007/s00604-019-3807-9.

59 D. Majumder and S. Roy, Non-fluorinated synthesis of anatase TiO_2 with dominant {001} facets: influence of faceted structures on formaldehyde sensitivity, *New J. Chem.*, 2017, **41**(15), 7591–7597, DOI: 10.1039/C7NJ00648A.

60 H. C. Choi, Y. M. Jung and S. B. Kim, Size effects in the Raman spectra of TiO_2 nanoparticles, *Vib. Spectrosc.*, 2005, **37**(1), 33–38, DOI: 10.1016/j.vibspec.2004.05.006.

61 A. Junkaew, M. Ehara, L. Huang and S. Namuangruk, Facet-dependent catalytic activity of anatase TiO_2 for the selective catalytic reduction of NO with NH_3: a dispersion-corrected density functional theory study, *Appl. Catal., A*, 2021, **623**, 118250, DOI: 10.1016/j.apcata.2021.118250.

62 A. Kumar Reddy Police, S. V. Prabhakar Vattikuti, Y.-J. Baik and B. Chan, Eco-friendly, hydrogen fluoride-free, morphology-oriented synthesis of TiO_2 with exposed (001) facets, *Ceram. Int.*, 2019, **45**(2), 2178–2184, DOI: 10.1016/j.ceramint.2018.10.128.

63 Q. Cheng, *et al.*, Rapid Hydroxyl Radical Generation on (001)-Facet-Exposed Ultrathin Anatase TiO_2 Nanosheets for Enhanced Photocatalytic Lignocellulose-to-H_2 Conversion, *ACS Catal.*, 2022, **12**(3), 2118–2125, DOI: 10.1021/acscatal.1c05713.

64 H. H. Hammud, H. Traboulsi, R. K. Karnati and E. M. Bakir, Photodegradation of Congo Red by Modified P25-Titanium Dioxide with Cobalt-Carbon Supported on SiO_2 Matrix, DFT Studies of Chemical Reactivity, *Catalysts*, 2022, **12**(3), 248, DOI: 10.3390/catal12030248.

65 T.-Y. Lee, C.-Y. Lee and H.-T. Chiu, Enhanced Photocatalysis from Truncated Octahedral Bipyramids of Anatase TiO_2 with Exposed {001}/{101} Facets, *ACS Omega*, 2018, **3**(8), 10225–10232, DOI: 10.1021/acsomega.8b01251.

66 N. Roy, Y. Park, Y. Sohn, K. T. Leung and D. Pradhan, Green Synthesis of Anatase TiO_2 Nanocrystals with Diverse Shapes and their Exposed Facets-Dependent Photoredox Activity, *ACS Appl. Mater. Interfaces*, 2014, **6**(19), 16498–16507, DOI: 10.1021/am504084p.

67 Z. Liu, *et al.*, mpg-C_3N_4/anatase TiO_2 with reactive {001} facets composites to enhance the photocatalytic activity of organic dye degradation, *RSC Adv.*, 2016, **6**(59), 54215–54225, DOI: 10.1039/C6RA06730A.

68 A. Gul, R. Ullah, J. Sun, T. Munir and S. Bai, The fabrication of TiO_2-supported clinoptilolite via F− contained hydrothermal etching and a resultant highly energetic {001} facet for the enhancement of its photocatalytic activity, *RSC Adv.*, 2021, **11**(29), 17849–17859, DOI: 10.1039/D1RA02269E.

69 A. K. John and S. Palaty, Green synthesis of nitrogen-doped TiO_2 nanoparticles with exposed {001} facets using Chromolaena odorata leaf extract for photodegradation of pollutants under visible light, *Nano-Struct. Nano-Objects*, 2024, **40**, 101402, DOI: 10.1016/j.nanoso.2024.101402.

70 H. Kaur, S. Kumar, G. Kaur, N. Kaur, R. Badru and R. Saini, An emerging expanse: Novel and eco-friendly-biogenic synthesis of *E. cardamomum*-wrapped TiO_2 nanoparticles for environmental and biological applications, *Environ. Res.*, 2023, **234**, 116599, DOI: 10.1016/j.envres.2023.116599.

71 A. Wojciechowska, A. Markowska-Szczupak and Z. Lendzion-Bieluń, TiO_2-Modified Magnetic Nanoparticles (Fe_3O_4) with Antibacterial Properties, *Materials*, 2022, **15**(5), 1863, DOI: 10.3390/ma15051863.

72 D. Mitoraj, *et al.*, Visible light inactivation of bacteria and fungi by modified titanium dioxide, *Photochem. Photobiol. Sci.*, 2007, **6**(6), 642–648, DOI: 10.1039/b617043a.

73 W. Zhou, C. Li, C. Sun and X. Yang, Simultaneously determination of trace Cd^{2+} and Pb^{2+} based on l-cysteine/graphene modified glassy carbon electrode, *Food Chem.*, 2016, **192**, 351–357, DOI: 10.1016/j.foodchem.2015.07.042.

74 P. Gupta, *et al.*, Parts per trillion detection of heavy metals in as-is tap water using carbon nanotube microelectrodes, *Anal. Chim. Acta*, 2021, **1155**, 338353, DOI: 10.1016/j.aca.2021.338353.

75 Y. He, Z. Wang, L. Ma, L. Zhou, Y. Jiang and J. Gao, Synthesis of bismuth nanoparticle-loaded cobalt ferrite for electrochemical detection of heavy metal ions, *RSC Adv.*, 2020, **10**(46), 27697–27705, DOI: 10.1039/D0RA02522D.

76 S. Wu, K. Li, Z. Zhang and L. Chen, Synthesis of imprinted chitosan/AuNPs/graphene-coated MWCNTs/Nafion film for detection of lead ions, *New J. Chem.*, 2020, **44**(33), 14129–14135, DOI: 10.1039/D0NJ02522D.

77 S. Kumar, S. Aftab, T. Singh, M. Kumar, S. Kumar and Y. Seo, Charge storage improvement in uniformly grown TiO_2 on $Ti_3C_2T_x$ MXene surface, *J. Alloys Compd.*, 2023, **968**, 172181, DOI: 10.1016/j.jallcom.2023.172181.

78 Y. Zhang, *et al.*, Highly sensitive detection of Pb^{2+} and Cu^{2+} based on ZIF-67/MWCNT/Nafion-modified glassy carbon electrode, *Anal. Chim. Acta*, 2020, **1124**, 166–175, DOI: 10.1016/j.aca.2020.05.023.

79 V. Oliveira, *et al.*, A sensitive electrochemical sensor for Pb^{2+} ions based on ZnO nanofibers functionalized by L-cysteine, *J. Mol. Liq.*, 2020, **309**, 113041, DOI: 10.1016/j.molliq.2020.113041.

80 L. Durai and S. Badhulika, Ultra-selective, trace level detection of As^{3+} ions in blood samples using PANI coated $BiVO_4$ modified SPCE via differential pulse anode stripping voltammetry, *Mater. Sci. Eng., C*, 2020, **111**, 110806, DOI: 10.1016/j.msec.2020.110806.

81 C. Xu, *et al.*, Biomass derived worm-like nitrogen-doped-carbon framework for trace determination of toxic heavy metal lead(II), *Anal. Chim. Acta*, 2020, **1116**, 16–26, DOI: 10.1016/j.aca.2020.04.033.

82 S. K. Sivan, *et al.*, Fabrication of a Greener TiO_2@Gum Arabic-Carbon Paste Electrode for the Electrochemical Detection of Pb^{2+} Ions in Plastic Toys, *ACS Omega*, 2020, **5**(39), 25390–25399, DOI: 10.1021/acsomega.0c03781.

83 J. Milikić, M. Savić, A. Janošević Ležaić, B. Šljukić and G. Ćirić-Marjanović, Electrochemical Sensing of Cadmium and Lead Ions in Water by MOF-5/PANI Composites, *Polymers*, 2024, **16**(5), 683, DOI: 10.3390/polym16050683.

84 Z. Liu, *et al.*, An Electrochemical Sensor for Detection of Lead(II) Ions Using Biochar of Spent Coffee Grounds Modified by TiO_2 Nanoparticles, *Molecules*, 2024, **29**(23), 5704, DOI: 10.3390/molecules29235704.

85 H. ma, *et al.*, A study of the photodeposition over Ti/TiO_2 electrode for electrochemical detection of heavy metal ions, *Electrochem. Commun.*, 2015, **57**, 18–21, DOI: 10.1016/j.elecom.2015.04.015.

86 V. P. Jyothilakshmi, R. Manu and S. Swaminathan, The fabrication of TiO_2/AgCNF/Nafion/GC electrodes for simultaneous electrochemical detection of Cd(II), Pb(II), Cu(II), and Hg(II) by optimizing the porosity of electrospun TiO_2 nanofibers, *J. Appl. Electrochem.*, 2024, **54**(10), 2377–2387, DOI: 10.1007/s10800-024-02110-2.

87 R. H. R. Mohammed, R. Y. A. Hassan, R. Mahmoud, A. A. Farghali and M. E. M. Hassouna, Electrochemical determination of cadmium ions in biological and environmental samples using a newly developed sensing platform made of nickel tungstate-doped multi-walled carbon nanotubes, *J. Appl. Electrochem.*, 2024, **54**(3), 657–668, DOI: 10.1007/s10800-023-01976-y.

88 A. M. Elsayed, A. M. Ahmed, M. T. Tammam, M. F. Eissa and A. H. Aly, Sensing of heavy metal Pb2+ ions in water utilizing the photonic structure of highly controlled hexagonal TiON/TiO_2 nanotubes, *Sci. Rep.*, 2024, **14**(1), 1015, DOI: 10.1038/s41598-023-50428-2.